L- AND C-BAND SAR INTERFEROMETRY ANALYSIS OF THE WIELICZKA SALT MINE AREA (UNESCO HERITAGE SITE, POLAND)

D. O. Nitti [1,2], F. Bovenga [3], A. Refice [3], J. Wasowski [4], D. Conte [1], R. Nutricato [1]

[1] Dipartimento Interateneo di Fisica, Politecnico di Bari, Italy
[2] DEOS - Delft University of Technology, Delft, The Netherlands
E-mail: [conte , nitti]@fisica.uniba.it , raffaele.nutricato@tiscali.it
[3] CNR ISSIA, Bari, Italy E-mail: [bovenga , refice]@ba.issia.cnr.it
[4] CNR IRPI, Bari, Italy E-mail: j.wasowski@ba.irpi.cnr.it

ABSTRACT

This work presents first results of interferometric processing of ALOS PALSAR Single Look Complex SAR images (Stripmap Single Polarization Mode), concerning ground deformations in the Wieliczka Salt Mine area, a few km from Cracow, Poland.

It follows a recent Persistent Scatterers SAR Interferometry (PSI) analysis on this area, obtained by processing several tens of ERS satellite images covering the period 1992-2000. The results revealed the presence of a few kilometres long, slowly subsiding zone corresponding very well to the extent of the underground salt mine. The present work aims to extend the analysis by exploiting ALOS-PALSAR data especially for the neighbouring rural areas, relying on the lower sensitivity to temporal decorrelation of L-band w.r.t. C-band radar data. Use of L band data is of interest because it could allow detecting faster ground movements related to sudden subsidence events that have occasionally occurred in the recent past. One such event, reported in the 1990's, caused ground displacements locally exceeding 3 m. Furthermore, with L-band SAR data some useful information can be obtained for the rural areas, which neighbour the salt mine but lack PS.

We present results obtained from Fine Beam, HH Single Polarization Mode (FBS), 34.3° Off-Nadir look-angle SAR images. The night acquisition time of FBS PALSAR images mitigates the atmospheric phase screen in each interferogram. No clear evidence of displacements is found on ALOS interferograms spanning about 1 year. The relatively high coherence shown by the interferograms allows easier unwrapping of the differential interferometric phase, aiding further statistical investigations on the spatial properties of the atmospheric signal.

We also present considerations concerning some processing aspects of ALOS data, as well as a preliminary comparison between the L-band and C-band differential interferometric phase behaviour.

1 INTRODUCTION

Wieliczka, a town located 14 km SE of Cracow, is home to a unique salt mine, over 700 years old, one of the best known tourist attractions in Poland. Each year the mine is visited by about 1 million tourists from all over the world and in 1978 UNESCO placed it on its first International List of the World Cultural and Natural Heritage.

First Persistent Scatterers SAR Interferometry (PSI) analysis on this area has been recently derived [1] by processing, through the PSI SPINUA [2] technique, 39 ERS-1/2 descending acquisitions covering the period 1992-2000. Numerous radar targets (over 100 PS/km^2) have been identified, allowing ground motion monitoring in the Wieliczka area (see Fig. 2). In particular, the results showed the presence of continuous subsidence with average movements ranging from about 1 to 2 cm/yr in the period 1992-2000. The detected width of the subsiding zone corresponds very well to the extent of the underground salt mine, whereas its length (around 4.5 km) is somewhat shorter with respect to that of the mining works and of the known salt deposit (Fig. 3). This discrepancy results in part from the lack of suitable radar targets in the rural areas east and west of the town of Wieliczka. The maximum downward displacements were observed in the western part of the town (up to 2.4 cm/yr), where the PS pattern is indicative of the presence of a few km long subsidence bowl. The ground topographic measurements in this area documented about 1 m of subsidence in the period 1970-2000 i.e. 3 cm/yr on average (The Wieliczka Salt Mine, unpublished

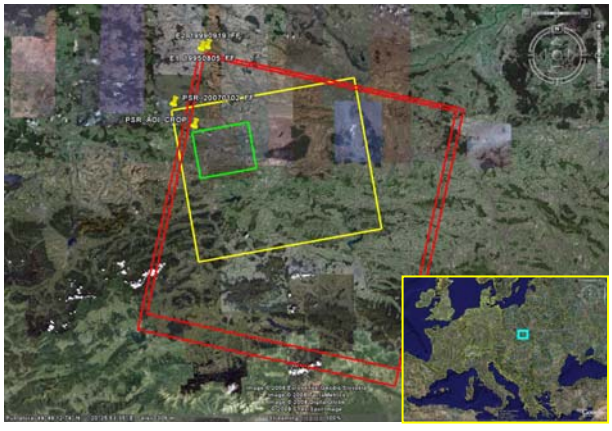

Figure 1. Yellow frame refers to the ALOS PALSAR acquisition (PRS_70070102), green frame encloses the AOI, red frames refer to ERS acquisitions E1_19950805 and E2_19990919. Inset shows the location of the study area.

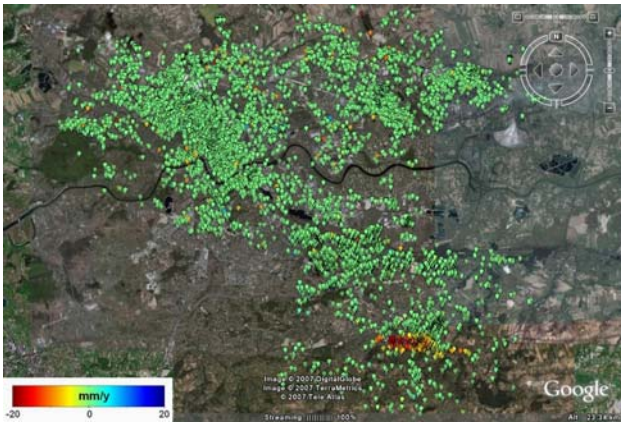

Figure 2. Geo-coded Persistent Scatterers (PS) distribution in the Cracow-Wieliczka area. Background optical image is from Google Earth™. Color represents the average Line of Sight (LOS) velocity (for the period 1992-2000). Note the predominance of motionless PS in the city of Cracow (upper part of the figure) and the presence of downward moving PS in the town of Wieliczka.

data). The slightly lower rates of PS displacements revealed for the period 1992-2000 can be in part explained by the ERS satellite LOS geometry.

There are also indications of possible linkages between the mine-induced subsidence and the presence of relatively large landslides occurring on the north facing slopes in the Wieliczka area.

Finally, there is evidence that the mining legacy has had a negative influence on the ground and building stability in the town, which is sited directly above the mine. Therefore, the subsidence hazard to houses and infrastructures in the Wieliczka area should be further monitored.

In the present study we extend the investigation of the Wieliczka mine area through use of L-band ALOS data. The aim is to cover rural or vegetated area where C-band decorrelate and PS-like targets are very few. Moreover, episodic occurrences of fast subsidence (from tens of cm to a few meters per year) in the recent past cannot be *a priori* ruled out, but they could not be unambiguously detected with C-band data, thus further motivating this L-band SAR application effort.

2 ALOS L-BAND INSAR

The Advanced Land Observing Satellite (ALOS) is a Japanese multi-sensor mission for remote sensing, recently launched into orbit (launch date: Jan. 24, 2006). Among the instruments onboard, the Phased Array type L-band Synthetic Aperture Radar (PALSAR) is the SAR sensor for day-and-night and all-weather land observation, that follows the one onboard the Japanese Earth Resources Satellite-1 (JERS-1) mission. The improved orbital accuracy (< 1 m) of ALOS w.r.t. JERS-1 ensures now a periodic global InSAR monitoring, thus representing a new instrument for the investigation of geophysical phenomena through interferometric techniques or, at least, contributing to their better understanding, through the comparison with the results obtained in different radar bands, like C-band (ERS and

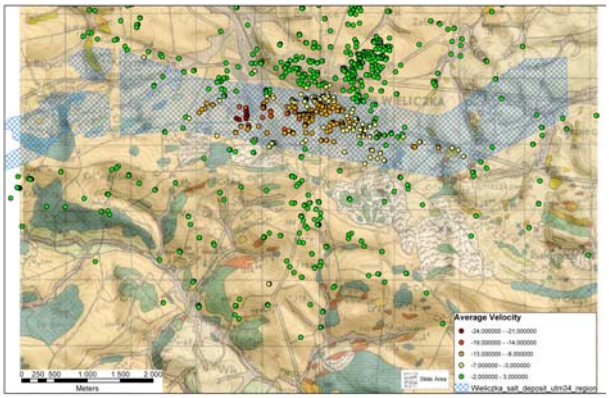

Figure 3. Geo-coded PS distribution superimposed on the geological map (http://www.pgi.gov.pl.) of the Wieliczka area draped over a DEM (after [1]*). Salt deposit (blue hatched pattern) occurs within the Miocene age sedimentary units, mantled in the Wieliczka depression by Quaternary sediments* [3]*. Note also the presence of relatively large landslides on the N-NNE facing slopes of the Carpathian mountain front (involving the Jurassic-Cretaceous flysch units).*

ENVISAT missions).

One of the advantages of L-band SAR data (wavelength $\lambda = 23.6$ cm for ALOS) w.r.t. C-band ($\lambda = 5.6$ cm for ERS) is the intrinsic capability to detect faster ground movements without ambiguities. Assuming a repeat-pass interval δt coincident with the ALOS orbital repeat cycle (46 days), we have a maximum detectable displacement rate along the line of sight (LOS) $v_{max} = \lambda/(4\delta t) = 46.8$ cm/yr, compared to the value of 14.6 cm/yr valid for the C-band ERS/ENVISAT missions, where the orbital repeat cycle is 35 days.

Furthermore, the longer the wavelength, the lower the temporal decorrelation of the interferometric phase [4]. Assuming an identical normal baseline, the geometrical decorrelation of an ALOS interferogram is also expected to be much lower than in C-band, because of the lower carrier frequency (Tab. 2) as well as the doubled chirp bandwidth of ALOS Fine Beam Single Polarization (FBS) acquisition mode w.r.t. ERS. The critical baseline reaches therefore ~15.4 km for ALOS-FBS (incidence angle $\theta_{inc} = 38.7°$), against only ~1.1 km for ERS. This implies that InSAR processing could be feasible for every pair of PALSAR acquisitions, since ALOS orbits should be controlled within a diameter tube of about 1 km since early 2007, (initially the diameter tube was 3 km [5]).

However, topographic residuals can be prominent in the differential interferometric phase, in case of interferograms with high perpendicular baselines $B_\perp$ (see Sect.5 below). Moreover, longer baselines require more care in image alignment on steep topography. This, together with the 2 times better slant range resolution of ALOS FBS images w.r.t. ERS, leads to local misregistrations, in case of uncompensated topography, that may become unacceptable (i.e., more than a 1/8 pixel). The benefits of a DEM-assisted approach for the coregistration of ALOS FBS images may be not negligible at all, in case of rough topography, as shown in [6].

Table 1. Processed ALOS stripmap acquisitions.

No	Scene Date	Orbit	Scene ID	Cycle	PRF (Hz)
1	2007/01/02	5015	ALPSRP050150990	8	2155.172
2	2007/02/17	5686	ALPSRP050686990	9	2132.196
3	2008/01/05	10383	ALPSRP103830990	16	2155.172
4	2008/02/20	11054	ALPSRP110540990	17	2132.196

The most significant disadvantages of L band w.r.t. C band are the influence of the ionosphere on the interferometric phase (ionospheric effects are expected to be more than 20 times stronger than in C band) and the 1.5 times worse InSAR slant range accuracy [5]

3 DATASET

All the ALOS PALSAR FBS Single-Look-Complex acquisitions planned by JAXA until February 2008 for the area of interest (AOI) have been processed (they are listed in Tab. 1). Fig. 1 shows the covered area on the ground for the ALOS full frame as well as the AOI, a 21×21 km^2 crop enclosing Wieliczka and Cracow.

In the following sections, the ALOS InSAR processing methodology will be described in detail, as well as the results obtained. Further investigations on the statistical properties of the phase of the generated ALOS interferograms will be attempted through cross-comparisons with a limited number of interferograms generated from the time series of ERS data described in [1], whose location, orientation, extent, polarization and resolution is summarized in Tab. 2, as well as those of the ALOS image stack.

4 ALOS INSAR PROCESSING

Differently than ERS, the pulse repetition frequency (PRF) of ALOS images may vary significantly along the track (between 1800 and 2200 Hz). In our case, for instance, PRF changes of more than 20 Hz are noticeable even for the same frame/track (Tab. 1). Therefore, for a proper image alignment, all the 4 ALOS acquisitions have to be first interpolated along azimuth direction in order to uniform the PRF.

Precise orbits are available for all the images and are stored in the leader file as 28 state vectors of position and velocity spaced at 60s intervals, 4 times wider than the full frame acquisition time extent (~16 s), thus enabling an Hermitian approach for the orbit interpolation [5]. Our tests highlight, indeed, errors in the interpolated satellite position along all the three Earth-Centred-Earth-Fixed (ECEF) reference system directions even exceeding one wavelength, if the state vectors velocity information is missed out, thus leading to non-negligible orbital residuals in the interferometric phase.

All ALOS FBS SLCs have been oversampled of a factor of 2 along the range direction, in order to have a square pixel on the ground.

After these pre-processing steps, the interferograms resulting from all the possible combinations among the ALOS SLCs available have been generated (Tab. 3). Range spectral shift compensation and azimuth common band filtering have been applied to improve the phase coherence by filtering out the not overlapping part of range and azimuth spectra. Azimuth common band filtering was not necessary, thanks to Doppler centroids never exceeding ±50 Hz (~2.3% of PRF) for all the processed images, thus denoting a very accurate yaw steering of the sensor.

DInSAR processing has been performed through the DORIS open source SAR interferometric processing tool [7] in order to produce a stack of differential interferograms.

Initially, a DTED-2 DEM of the area provided by the NASA Shuttle Radar Topography Mapping (SRTM) mission, with 3" posting in latitude and longitude and a vertical accuracy of ~15 m, has been used to estimate and remove the topographic component from the phase of the interferogram stack (2-Pass DInSAR).

Phase unwrapping of the differential interferometric phase was performed with SNAPHU (*Statistical-Cost, Network-Flow Algorithm for Phase Unwrapping* [8]). The method selected for the initialization is the Minimum Spanning Tree (MST). The coherence maps are used in the definition of the cost functions.

In order to detect and mask out potential unwrapping artefacts, the following iterative procedure was applied. A low-pass filtering of the wrapped phase is performed before unwrapping through a moving average window. For any interferogram, the wrapped differential phase φ_W is filtered independently with three different moving average windows of the following dimensions: 21×21 pixels (corresponding to about 100×100 m^2); 15×15 pixels (~75×75 m^2); and 11×11 pixels (~50×50 m^2). We denote these three datasets as $\varphi_{W,21}$, $\varphi_{W,15}$, and $\varphi_{W,11}$, respectively. Once the three filtered phase fields have been unwrapped ($\varphi_{W,21}\rightarrow\varphi_{21}$ $\varphi_{W,15}\rightarrow\varphi_{15}$ $\varphi_{W,11}\rightarrow\varphi_{11}$), all the pixels where a difference in the number of the estimated 2π cycles in any of the three phase fields is noticed are marked as potential artefacts and masked out. The optimal values for the moving average win-

Table 2. Parameters relevant to the stacks of ALOS and ERS processed images. A/D: ascending/descending pass direction; f_c: carrier frequency; λ: wavelength; B_W: chirp bandwidth; R_{gr}: ground range resolution; R_{az}: azimuth resolution; θ_{inc}: scene centre incidence angle; B_c: critical baseline, estimated for the specific beam and imaging mode

Sensor	Track	Frame	A/D	Pol.	f_c (GHz)	λ (cm)	B_W (MHz)	R_{gr} (m)	R_{az} (m)	θ_{inc} (°)	B_c (km)	Day / Night acquisition	Swath extent
ERS	179	2601	D	VV	5.3 (C band)	23.6	15.55	24.5	5	23.0	1.1	Day	100km
PALSAR	622	990	A	HH	1.27 (L band)	5.6	28.00	8.6	5	38.7	15.4	Night	70 km

dows sizes were found by trial and error; for smaller windows, the unwrapping artefacts become unacceptably large covering the entire AOI, especially on the interferograms with temporal baseline comparable to 1 year.

Once all the potential unwrapping artefacts have been masked out, orbital residuals are removed by modelling them over the AOI as a bilinear phase trend, estimated through a LMS fit with the unwrapped interferometric phase, by considering only those pixels with a coherence better than 0.3. Also, timing errors along range and azimuth directions have been precisely estimated and corrected for all the ALOS SLCs, by coregistering their intensity with the corresponding simulated power.

The phase of all the differential interferograms exhibits significant variability, in particular over Cracow, where a phase "blob" can be noticed, with maximum phase values increasing with the normal baseline, thus suggesting the presence of topographic residuals (Fig. 4A-B), related to the intrinsic finite vertical accuracy of the DEM. Indeed, this signal is stronger in the interferograms with height of ambiguity close to the DEM vertical accuracy, like those shown in Fig. 4.

In order to prove this assertion, 3-Pass interferograms have been generated for all the interferograms with a temporal baseline higher than 46 days, where the topographic interferogram is given by the two acquisitions of 2007 (B_t = 46 d, so minimizing the temporal decorrelation as well as the ground displacements), with a height of ambiguity lower than the corresponding value for the 2008 topographic interferogram.

As shown in Fig. 4C, the strong phase component over Cracow is not visible anymore, so providing a first confirmation about the hypothesis of topographic residuals. The processing steps for the 3-Pass DInSAR (unwrapping, detrending, masking) are identical to those described for the 2-Pass DInSAR.

5 RESULTS ANALYSIS

None of the processed interferograms with longer temporal baselines (about 1 year) shows clear evidence of movements, on or around the Wieliczka area. This rules out the occurrence of strong episodic deformation phenomena on the area during the year 2007.

Assuming that the deformation is continued during the year 2007 at the same rate evidenced by the PSI analysis in the interval 1992-2000, i.e. with maximum displacement rates of about 2.4 cm/yr, this maps on the LOS of the PALSAR sensor to about 2 cm/yr displacement rate. This displacement rate seems too small to be appreciable by an L-band sensor. To support this claim, we analyse in the following the various contributions to the interferometric phase in the PALSAR interferograms.

The InSAR phase can be explained in terms of residuals of i) topography, ii) atmospheric contribution (due to both troposphere and ionosphere) and iii) system noise.

5.1 Topography residual

In the hypothesis that the main contribution to the InSAR phase is the residual topography, it depends on the baseline $B_\perp$; therefore the difference between the InSAR

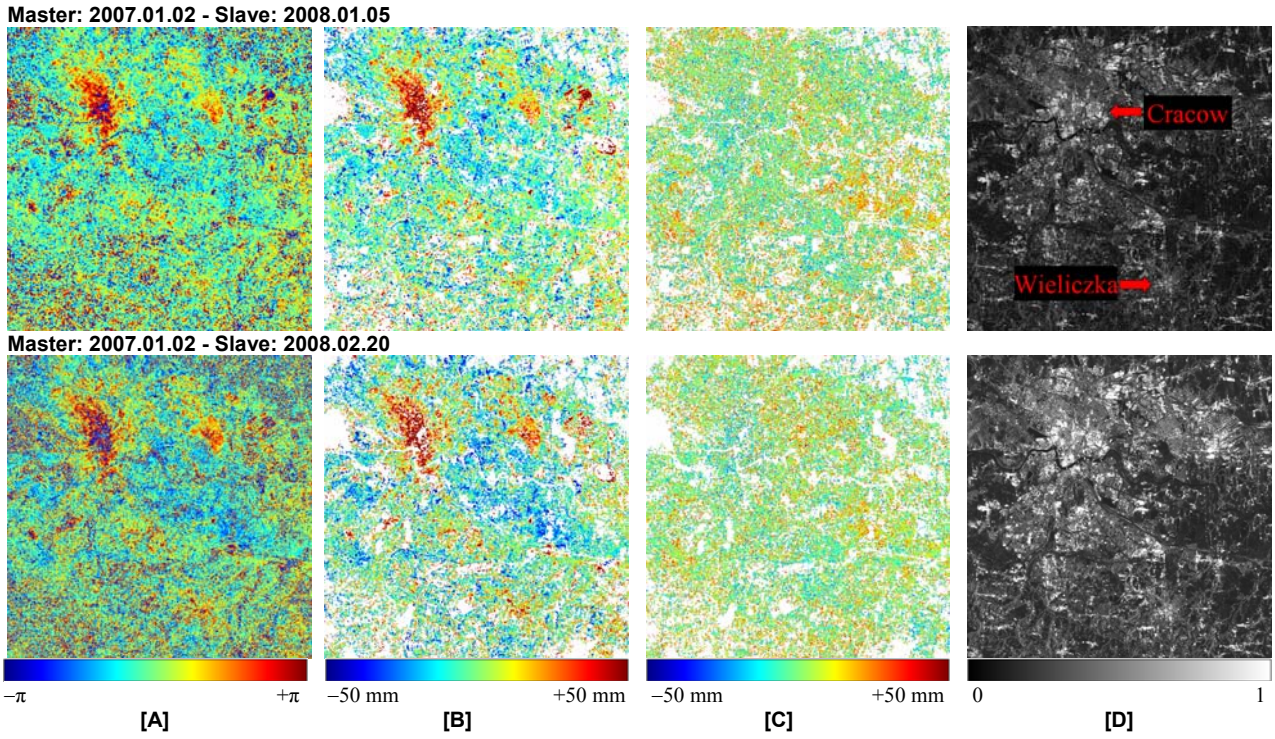

Figure 4. [A] 2-pass wrapped interferometric phase for 2 of the 6 interferograms generated; [B] corresponding 2-pass unwrapped interferometric phase, converted into LOS displacements. White areas have been masked out (unwrapping artefacts or coherence worse than 0.3). Spatial extent is that of the green rectangle in Fig. 1. [C] 3-pass unwrapped interferometric phase, converted into LOS displacements (topographic interferogram: 2007/01/02_2008/02/20). White areas are masked as in Fig. 4.B. [D] Interferogram magnitude.

Table 3. Parameters of the stack of ALOS interferograms. B_t: temporal baseline; $B_\perp$: normal baseline; H_a: height of ambiguity ; γ_g: theoretical geometric decorrelation. Mean, Median, Mode and standard deviation refer the values estimated on the corresponding coherence maps whose histograms are plotted in Fig. 7.

Interferogram		B_t [d]	$B_\perp$ [m]	H_a [m]	γ_g	Mean $<\gamma_{tot}>$	Median	Mode	Std.Dev.
Master	Slave								
2007/01/02	2007/02/17	46	1705.3	37.8	0.89	0.4143	0.43	0.497	0.1858
	2008/01/05	368	3671.7	17.6	0.76	0.1380	0.1115	0.080	0.1103
	2008/02/20	414	4568.0	14.1	0.7	0.1557	0.1255	0.084	0.1209
2007/02/17	2008/01/05	322	1967.4	32.7	0.87	0.1654	0.1325	0.088	0.1308
	2008/02/20	368	2864.0	22.5	0.81	0.1973	0.165	0.096	0.1432
2008/01/05	2008/02/20	46	896.6	71.9	0.94	0.3622	0.355	0.3440	0.1326

phase normalised w.r.t. $B_\perp$ should be close to zero. The plot in Fig. 5 shows the histograms of the residual topography, obtained from the (unwrapped) interferometric phase scaled by the spatial baseline, computed on the two independent 2-pass interferograms (blue and black curves), as well as the difference between the two (red curve). The latter appears to be peaked around zero more than the first two, thus proving the presence of a residual common topographic phase component in both the 2-pass datasets. This contribution vanishes in the 3-pass interferograms.

5.2 Atmospheric contribution

Statistical tests were performed concerning the spatial properties of the atmospheric signal. For phase fields given exclusively by turbulent tropospheric contribution, Kolmogorov turbulence theory predicts that the power spectrum of the phase signal follows a power law with exponents 5/3 and 2/3 for small and large scales, respectively [4]. The spectral phase behaviour can be investigated by computing the structure function (or variogram) of the residual phase fields Φ, $V_\varphi(d) = \left\langle [\Phi(p+d) - \Phi(p)]^2 \right\rangle$, where p denotes the pixel position and d is the distance between pixel pairs. In order to estimate robustly the variogram, only those pixels showing high interferometric coherence in all the residual phase fields were involved in the computation.
Fig. 6 shows the variograms of PALSAR 3-PASS differential interferometric phase fields (PSR_20070102_PSR_20080105 in red and PSR_20070102_PSR_20080220 in blue): neither plot shows evident power-law trend, thus excluding the presence of dominant tropospheric turbulent components in the interferometric phase fields. This is consistent with the fact that ALOS data have been acquired at night time (20h 57m) and during the winter season (January and February). On the contrary, the green line in Fig. 6, representing the variogram computed on an ERS tandem interferogram (E1_19950805_E2_19950806), exhibits relatively clear power-law behavior, close to the theoretical trends $\rho^{5/3}$ and $\rho^{2/3}$, which are sketched as dotted lines in the log-log diagram for reference. The ERS tandem pair has been chosen for this analysis in order to minimise the temporal decorrelation. ERS data have been acquired during daytime (9h 38m) in summer or autumn seasons when tropospheric turbulences can strongly affect the InSAR signal.
Concerning the contribution due to ionosphere, it is expected to be stronger in L than in C band. By expressing the path length contribution as a function of the total electron content (TEC) we have [4]:

$$\Delta l_{atm}^{Iono} = -\frac{40.28}{f_i^2 \cos(\theta_i)} \cdot \mathrm{TEC} \qquad (1)$$

$$\frac{\Delta l_{atm}^{Iono,L}}{\Delta l_{atm}^{Iono,C}} = \left(\frac{f_C}{f_L}\right)^2 \cdot \frac{\cos(\theta_C)}{\cos(\theta_L)} = 20.5 \qquad (2)$$

Table 4. Noise parameters of the two 1-year PALSAR interferograms. The last column reports the expected LOS displacement rate assuming the same trend as measured in the ERS time series analysis.

Interferogram	Phase rms (rad)	Slant range rms (mm)	Expected *dR* (mm/yr)
PSR_20070102_PSR_20080105	1.07	20.09	20
PSR_20070102_PSR_20080220	1.05	19.82	23

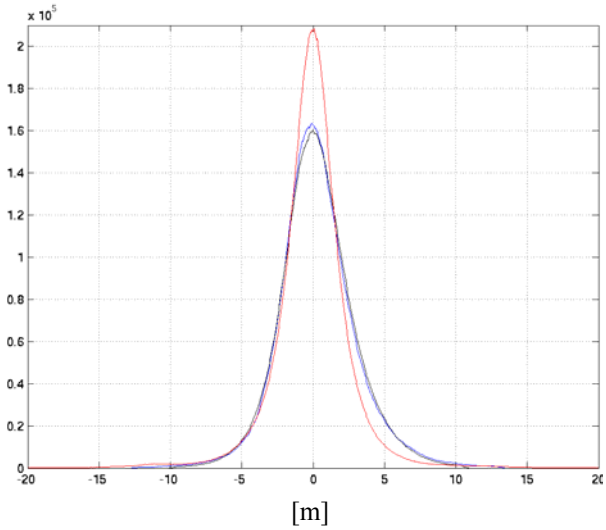

Figure 5. *Histograms of the residual topography computed by using the 2-pass interferograms (blue, green) and the difference between the two estimates (red).*

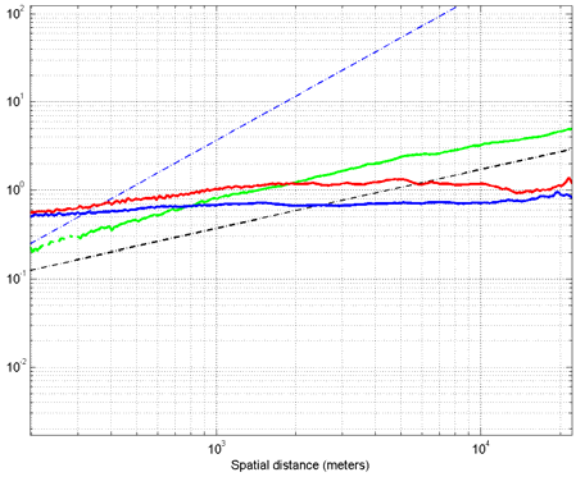

Figure 6. Variograms of residual PALSAR phase fields PSR_20070102_PSR_20080105 (red), PSR_20070102-_PSR_20080220 (blue) and ERS E1_19950805_E2_-19950806 (green line). The theoretical power laws $\rho^{5/3}$ and $\rho^{2/3}$ are represented by the dotted lines.

where f_i is the carrier frequency, θ_i the incident angle and TEC the total electron content of the ionosphere. The last equality in (2) is obtained by using the actual values of the incidence angle for ALOS (38.7°) and ERS (23.2°), as well as the respective carrier frequencies. However, due to the fact that the SAR image have been acquired during night time (20h 57m) the TEC value drops to zero and the influence of this atmospheric contribution can be neglected.

5.3 Noise floor

Having ruled out the presence of either topographic or atmospheric residuals, we can evaluate the noise floor of the Interferometric measurements by computing the rms of the residual InSAR phase: $\sigma_R = (\lambda/4\pi)\sigma_\phi$. The rms has been computed on the residual InSAR phase fields obtained through 3-pass processing. As mentioned, the processing required a spatial filtering in order to perform robust phase unwrapping. The resultant slant range rms values are reported in Tab. 4. Values about 4 to 6 times smaller were obtained in [5], where PALSAR interferograms with proportionally smaller spatial and temporal baselines were analysed. The difference can thus be explained in terms of different spatial and temporal decorrelation contributions.

The above considerations give us confidence on the value of the estimated noise floor on our two 1-year interferograms. This value is in fact barely sufficient to detect displacement rates of the same magnitude of those measured by ERS in 1992 – 2000.

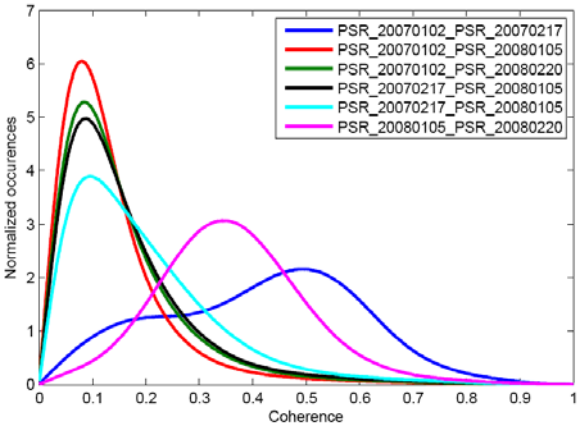

Figure 7. Histograms of the coherence values computed on the six ALOS interferograms. First order statistics (mean, median, mode) and standard deviations are listed in Tab. 3.

6 TEMPORAL DECORRELATION

As a final exercise, we attempt a modelling of the temporal decorrelation phenomenon on our PALSAR data. An exponential decay model is often used to describe the temporal decorrelation behaviour [9]:

$$\gamma_t = \exp\left(-\frac{|B_t|}{T}\right), \tag{3}$$

where T is a temporal decay constant that depends on both the surface coverage of the area under study and the radar wavelength.

Fig. 7 shows the coherence histograms for all the ALOS interferograms generated. Basic statistics on their coherence maps, such as mean, median, mode and standard deviation, are listed in Tab. 3.

We then estimated T for our ALOS data as the rate of the straight line defined by:

$$\ln(\gamma_t) = -\frac{1}{T}|B_t| \tag{4}$$

in a semi-log plot, where γ_t has been computed as:

$$\gamma_t = \frac{\langle \gamma_{tot} \rangle}{\gamma_g}. \tag{5}$$

The decay constant, fitted on the data from all the six 2-pass interferograms (see Fig. 8), is about 475 days. Further analyses, through processing of higher numbers of ALOS images, should allow a better characterization of this parameter, which is of interest for an assessment of InSAR feasibility with ALOS.

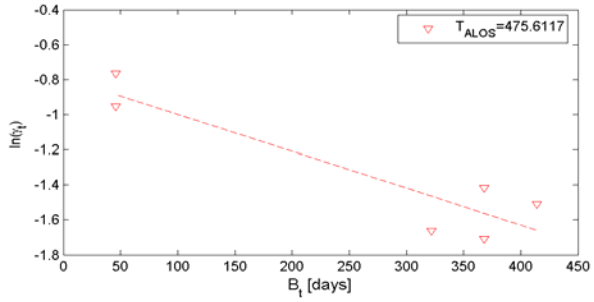

Figure 8. Temporal coherence trends estimated for the six ALOS interferograms. The T value refers to the parameter in Eq.3 estimated on the data.

7 CONCLUSIONS

We have used L-band ALOS PALSAR data acquired in 2007-2008 to investigate the Wieliczka, Poland, test site, which was recently investigated through PSI techniques on ERS time series. Four PALSAR HH scenes were processed interferometrically to derive six 2-pass interferograms. These were also combined into 3-pass interferograms. The interferograms spanning 1 year do not show any clear evidence of displacements on the Wieliczka area. This rules out the occurrence of strong terrain movements in the period.

Through accurate analysis and modelling of topographic, atmosphere and temporal decorrelation phenomena, we arrive at an estimation of the noise floor of DInSAR measurements on our dataset which is in line with other evaluations reported in the literature. It can then be concluded that movements of the same magnitude as those detected by PSI investigations are barely below the sensitivity threshold of our PALSAR interferograms.

From a more general point of view, it can be concluded that L-band and C-band InSAR can play a complementary role in deformation monitoring, especially in view of the following considerations:

- C-band data allow to detect precisely small displacement rates, while L-band data are more sensitive to strong deformation episodes, for which C band is beyond the aliasing limit;
- Availability of long historical data records enable application of PSI techniques in C band, thus reaching single-pixel precision, while the reduced geometrical decorrelation in L band favors easier application of conventional interferometry based on distributed scatterers, allowing coverage of larger areas with few man-made features, where PSI methods fail.

Future work will concentrate on the following aspects:

- further ALOS PALSAR data processing, possibly involving more scenes;
- further investigations on the coherence aspects;
- investigations about the availability of other data such as X-band for further comparisons (definition of a “super site” for L-C-X band InSAR application studies).

ACKNOWLEDGEMENTS

PALSAR satellite images were provided by ESA under the ALOS ADEN AO 3595 project.

REFERENCES

[1] Wasowski, J., Bovenga, F., Nutricato, R., Conte, D., Refice, A., Kowalski, Z. & Graniczny M. (2007). Satellite interferometry reveals spatial patterns of subsidence in the ancient Wieliczka Salt Mine (UNESCO Heritage Site, Poland). *In Proceedings of FRINGE, Frascati, Italy, Nov.26–30, 2007.*

[2] Bovenga F., Refice A., Nutricato R., Guerriero L. & Chiaradia M.T. (2004). SPINUA: a flexible processing chain for ERS / ENVISAT long term interferometry. *In Proceedings of ERS-ENVISAT Symposium, 6-10 Sept. 2004, Salzburg, Austria.*

[3] Kolasa K. & Slaczka, A. (1985). Sedimentary saltmegabreccias exposed in the Wieliczka mine, Fore-Carpathian Depression. *Acta Geol. Colonica.* **35**, 221-230.

[4] Hanssen, R. F. (2001). Radar Interferometry: Data Interpretation and Error Analysis. *Kluwer Academic Publishers, Dordrecht.*

[5] Sandwell D., Myer D., Mellors R., Shimada M., Brooks B. & Foster J. (2007). Accuracy and Resolution of ALOS Interferometry: Vector Deformation Maps of the Father's Day Intrusion at Kilauea. *IEEE Trans. Geosci. Rem. Sens.*, 2007-00737.R1. (On-line: http://topex.ucsd.edu/sandwell/publications/117_GRS_ALOS_accuracy.pdf)

[6] Nitti D.O., Hanssen R.F., Refice A., Bovenga F., Milillo G. & Nutricato R. (2008). Evaluation on DEM-assisted SAR coregistration. In *Proceedings of SPIE Remote Sensing, 15–18 Sept. 2008, Cardiff, Wales, United Kingdom.*

[7] Kampes B., Hanssen R. & Perski Z. (2003). Radar Interferometry with Public Domain Tools. In *Proceedings of FRINGE*, Frascati, Italy, Dec. 1-5, 2003.

[8] Chen C. W. & Zebker H. A. (2002). Phase unwrapping for large SAR interferograms: Statistical segmentations and generalized network models. *IEEE Transactions on Geoscience and Remote Sensing*. **40**(8), 1709-1719.

[9] Zebker H. and Villasenor, J. (1992). Decorrelation in interferometric radar echoes. *IEEE Trans. on Geoscience and Remote Sensing*. **30**(5), 950-959.